Sooran Noroozi[1]

Seyed Hassan
Hashemabadi[1]

[1] Computational Fluid
Dynamics Research
Laboratory, School of Chemical
Engineering, Iran University of
Science and Technology,
Tehran, Iran.

Research Article

CFD Simulation of Inlet Design Effect on Deoiling Hydrocyclone Separation Efficiency

An Eulerian-Eulerian three-dimensional CFD model was developed to study the effect of different inlet designs on deoiling hydrocyclone separation efficiency. Reynolds averaged Navier Stokes and continuity equations were applied to solve steady turbulent flow through the cyclone with the Reynolds stress model. In addition, the modified drag correlation for liquid-liquid emulsion with respect to the Reynolds number range and viscosity ratio of two phases was used and the simulation results were compared with those predicted by the Schiller-Naumann correlation. Pressure profile, tangential and axial velocities and separation efficiency of the deoiling hydrocyclone were calculated for four different inlet designs and compared with the standard design. The simulation results for the standard design demonstrate an acceptable agreement with reported experimental data. The results show that all new four inlet designs offer higher efficiencies compared to the standard design. The difference between the efficiency of the LLHC, of the new inlets and the standard design can be improved by increasing the inlet velocity. Furthermore, the simulations show that the separation efficiency can be improved by about 10 % when using a helical form of inlet.

1 Introduction

Hydrocyclones are widely used as separators, degassers and mass transfer devices in many fields such as the mineral, petroleum, textile and petrochemical industries. The specific features of hydrocyclones like low maintenance costs, easy operation and installation make them appropriate for separation processes. Several experimental and computational investigations have been conducted to determine the effects of design parameters on the separation efficiency and flow structure.

The most common application of long hydrocyclones as liquid-liquid separators is the oil separation from wastewater emulsions in the oil industry. The analysis of complex swirl fluid flow through the liquid-liquid hydrocyclone (LLHC) was studied theoretically and experimentally [1–3]. Due to the fact that the exploration of new designs is time-consuming and costly to do by experimentation, several attempts have been made to simulate the solid-liquid hydrocyclone (SLHC) with CFD techniques for different geometries and some CFD simulations of deoiling hydrocyclones have been reported. Grady et al. [4] made use of the Reynolds stress turbulence closure model and the algebraic slip multiphase model to predict the velocity field and separation efficiency of a 10 mm deoiling hydrocyclone. Paladino et al. [5] applied the same approaches to simulate the multiphase flow behavior for low concentration of oil in the hydrocyclone feed. Huang [6] used the Reynolds stress model (RSM) to model turbulence flow and the Eulerian-Eulerian approach to predict the phase behavior for high concentration of oil in the feed of a Coleman-Thew type hydrocyclone by two inlets. The inlet design has noticeable effects on energy saving and the centrifugal force of fluid flow at the feed entrance of a hydrocyclone. So, the inlet configuration is an important parameter in the performance of a LLHC. Chu et al. [7] considered the effect of body and inlet design of a hydrocyclone on separation efficiency. They experimentally studied the energy loss in different geometrical parts of a SLHC. Olson and Ommen [8] employed the algebraic slip mixture model and the Reynolds stress turbulence model to simulate new inlet designs and compared the results in percent of recovery using CFD with the standard design results for a SLHC.

Correspondence: Asst. Prof. S. H. Hashemabadi (hashemabadi@iust.ac.ir), Computational Fluid Dynamics Research Laboratory, School of Chemical Engineering, Iran University of Science and Technology, 16846, Tehran, Iran.

The influence of inlet design on the performance of a deoiling hydrocyclone has not been reported before, neither experimentally nor numerically. In the current work, the effect of different inlet designs on the separation efficiency of a typical deoiling hydrocyclone was studied using CFD techniques and the results were compared with those of the standard design.

2   Governing Equations

2.1   Liquid-Liquid Flow Simulation Approach

To model a highly turbulent fluid flow through a hydrocyclone, the Reynolds averaged continuity and motion equations were solved simultaneously with Reynolds stress turbulence model equations.

The algebraic slip mixture (ASM) model and the Eulerian-Eulerian multiphase model have been previously used in the literature to simulate multiphase behavior in a deoiling hydrocyclone. The ASM model is a simplification of the Eulerian approach used for multiphase flow. The ASM approach for dispersed phase flow allowed consideration of the problem at low computational cost in relation to the Eulerian-Eulerian approach. In this model the transfer equations are solved for the multiphase mixture and then the slip velocity and drift velocity for each phase are described by algebraic equations. In the Eulerian-Eulerian multiphase model, however, each phase is treated as a continuum and characterized by averaged conservation equations; so this model is more accurate than the ASM model. Owing to this fact, the liquid-liquid two-phase flow is described by using the Eulerian-Eulerian approach. For incompressible fluids, the averaged continuity and momentum equations for each phase (oil or water) may be obtained from the following equations[1]:

$$\frac{\partial\left(\bar{a}_p\rho_p\right)}{\partial t} + \nabla.\left(\bar{a}_p\rho_p\bar{u}_p\right) = 0 \tag{1}$$

$$\frac{\partial\left(\bar{a}_p\rho_p\bar{u}_p\right)}{\partial t} + \bar{u}_p\nabla.(\bar{a}_p\rho_p\bar{u}_p)$$
$$= -\bar{a}_p\nabla P - \nabla.\left[\bar{a}_p(\tau_p^l + \tau_p^t)\right] + \bar{a}_p\rho_p g + F \tag{2}$$

where P is the static pressure and g is the gravitational body force. In the above equations subscript 'p' is replaced by 'c' for the continuous phase (water) or 'd' for the dispersed phase (oil), a is the phase fraction and F denotes the interphase momentum exchange terms between the continuous phase (water) and the dispersed phase (oil). In principle, the term 'F' should include all the related interphase forces. Since the lift force and the virtual mass force contribute little to the solution, they were ignored in the calculations. The interphase momentum transfer term may be obtained by the drag coefficient C_D from the following relationship:

---

1)   List of symbols at the end of the paper.

$$F = \frac{3\bar{a}_d\bar{a}_c\rho_c C_D|\bar{u}_d - u_c|(u_d - u_c)}{4d_d} \tag{3}$$

In liquid-liquid emulsion flows like those in a LLHC, the value of the drag coefficient (C_D) depends on the droplet Reynolds number and the viscosity ratio ($\kappa = \mu_d/\mu_c$) [9, 10]. Depending on whether slip or non-slip flow is assumed at the droplet interface, distinct formulations for estimating the drag coefficient are applied. For the pure droplet, there is slip flow along the interface which is driven by internal circulation that reduces the drag coefficient [11]. Due to this fact, the Hadamard-Rybcynski correlation [9] was used to estimate the drag coefficient for the creeping flow ($Re_d < 1$). In addition, the numerically based correlation proposed by Rivikind and Ryskin [12] was employed in the Reynolds number range of 1–500. For higher Reynolds numbers, the drag coefficient was set to 0.44. Therefore, the modified drag coefficient is:

$$C_D = \begin{cases} \frac{8}{Re_d}\left(\frac{3k+2}{k+1}\right) & Re_d \leq 1 \\ \frac{1}{1+k}\left[k\left(\frac{24}{Re_d} + 4Re_d^{-\frac{1}{3}}\right) + 14.9Re_d^{-0.78}\right] & 1 < Re_d \leq 500 \\ 0.44 & Re_d > 500 \end{cases} \tag{4}$$

where Re_d is the droplet Reynolds number:

$$Re_d = \frac{\rho_c|u_c - u_d|d_d}{\mu_c} \tag{5}$$

If the droplet is contaminated or the viscosity ratio approaches infinity ($k > 50$), the drag coefficient can be calculated as solid particle due to effectively no-slip condition on the particle surface. In these cases, the empirical Schiller-Naumann correlation can be used which is appropriate up to Reynolds number 1000 [11]:

$$C_D = \begin{cases} \frac{24}{Re_d}\left(1 + 0.15\,Re_d^{0.687}\right) & Re_d \leq 1000 \\ 0.44 & Re_d > 1000 \end{cases} \tag{6}$$

The coalescence, breakage and deformation of droplets were assumed to be negligible.

2.2   Turbulence Flow Model

The Reynolds stress model is one of the turbulence models based on Reynolds-averaged Navier–Stokes (RANS) equations. Since the Reynolds stress turbulence model accounts for the effects of streamline curvature, eddy, swirl, and quick changes in stress rate in a more rigorous manner, it has greater potential to accurately predict complex flows, as in the case of hydrocyclones. In the RSM, the eddy viscosity approach is discarded and the Reynolds stress components ($R_{k,ij}$) are calculated directly. The turbulence stress tensor $\left(\tau_k^t\right)$ can be defined as [4]:

$$\tau_k^t = -\rho_k R_k, ij, \qquad R_{k,ij} = \overline{\bar{u}_{k,i}\bar{u}_{k,j}} \tag{7}$$

The turbulence stress components ($R_{k,ij}$) can be obtained from the following partial differential equation:

$$\frac{\partial}{\partial t}\left(\bar{a}\rho R_{ij}\right) + \frac{\partial}{\partial x_l}\left(\bar{a}\rho \bar{u}_l R_{ij}\right) = P_{ij} + D_{ij} + \Phi_{ij} - \varepsilon_{ij} \qquad (8)$$

where P_{ij} is the production of turbulence by the mean strain and can be expressed by the formulation:

$$P_{ij} = -\rho\bar{a}\left(R_{il}\frac{\partial \bar{u}_j}{\partial x_l} + R_{jl}\frac{\partial \bar{u}_i}{\partial x_l}\right) \qquad (9)$$

The diffusion term (D_{ij}) which contains the molecular diffusion (D_{Lij}) and turbulent diffusion (D_{Tij}) can be written as:

$$D_{ij} = D_{Lij} + D_{Tij} = \frac{\partial}{\partial x_l}\left(\bar{a}\mu\frac{\partial R_{ij}}{\partial x_l}\right) + C_\mu\frac{\partial}{\partial x_l}\left(\bar{a}\frac{\mu_t}{\sigma_k}\frac{\partial R_{ij}}{\partial x_l}\right) \qquad (10)$$

The turbulence viscosity μ_t can be calculated by:

$$\mu_t = \rho C_s\frac{\kappa^2}{\varepsilon}, \quad \kappa = \frac{1}{2}R_{ij} \qquad (11)$$

Using the Kolmogrov assumption of local isotropy, the dissipation rate tensor (ε_{ij}) can be expressed as:

$$\varepsilon_{ij} = \frac{2}{3}\varepsilon\bar{a}\rho\delta_{ij} \qquad (12)$$

where ε is the scalar turbulent dissipation rate and is given by:

$$\frac{\partial(\rho\bar{u}_l\varepsilon)}{\partial x_l} = \frac{\partial}{\partial x_l}\left(C_\varepsilon\rho\frac{\varepsilon}{\kappa}R_{ij}\frac{\partial\varepsilon}{\partial x_j}\right) + \frac{\varepsilon}{\kappa}\left(-2C_{\varepsilon 1}\rho R_{ij}\frac{\partial\bar{u}_i}{\partial x_l} - C_{\varepsilon 2}\rho\varepsilon\right) \qquad (13)$$

Φ_{ij} is the redistribution of turbulence by the pressure strain. The pressure strain correlation plays an important role in the Reynolds stress model. For modeling the pressure strain different alternatives have been presented in the literature. In this work, the linear pressure strain correlation was used [13]:

$$\Phi_{ij} = \Phi_{ij1} + \Phi_{ij2} \qquad (14)$$

$$\Phi_{ij1} = -C_1\rho\frac{\varepsilon}{\kappa}\left(R_{ij} - \frac{2}{3}\delta_{ij}\kappa\right) \qquad (15)$$

where eight constants in the RSM equations are:

$$C_\mu = 0.24, C_1 = 1.8, C_2 = 0.6, C_{\varepsilon 1} = 1.44, C_{\varepsilon 2} = 1.92,$$
$$C_\varepsilon = 0.13, \sigma_k = 0.82, C_s = 0.09.$$

Thus, the Reynolds stress turbulence model is formulated by six partial differential equations of the Reynolds stress tensor components (see Eq. (8)) and one equation for the scalar turbulent dissipation rate (see Eq. (13)), in total seven partial differential equations.

3   Problem Identification

3.1   Standard Geometry and Mesh Generation

The standard hydrocyclone design used in this simulation has a diameter (D_s) of 40 mm for the cylindrical inlet chamber. Geometrical details of a typical deoiling hydrocyclone used in this study are illustrated in Fig. 1. For mesh independency, the efficiency results were verified by comparison with experimental work [14] for four different mesh densities (50000, 130000, 250000 and 315000) in three different droplet diameters (see Fig. 2). Tetrahedral unstructured cells were used in all simulations. The results show that predictions are better at higher mesh densities, but despite the small computational error (approx. 3.5 %) for results in 315000 mesh density in comparison with 250000 mesh density the computation time in this mesh density is much higher (approx. 18 % more) than in the 250000 mesh density, so 250000 computational cells have been implemented in this work as the optimal mesh density in computational time and accuracy in results. With the mentioned mesh, the average error of simulation for the diameter size 25 to 50 micron is approx. 16 % and the computational time with
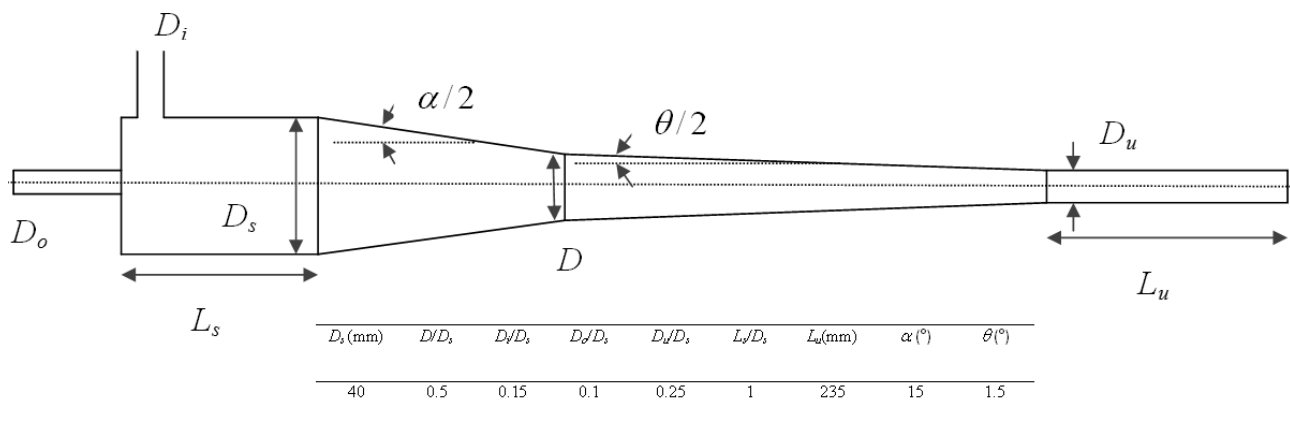

D_s (mm)	D/D_s	D_i/D_s	D_o/D_s	D_u/D_s	L_s/D_s	L_u (mm)	α (°)	θ (°)
40	0.5	0.15	0.1	0.25	1	235	15	1.5

Figure 1. Typical deoiling hydrocyclone design [19].

1888   S. Noroozi et al.

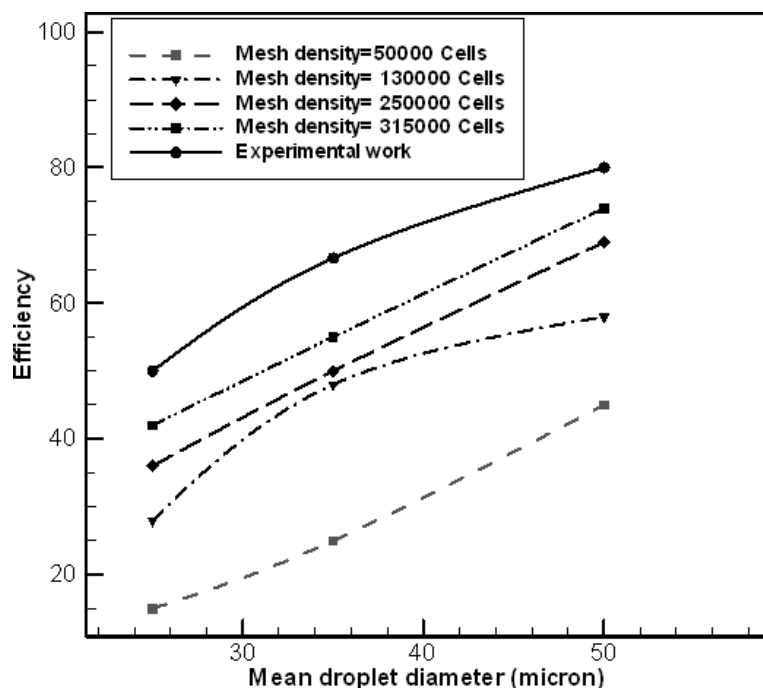*Chem. Eng. Technol.* **2009**, *32*, No. 12, 1885–1893

Figure 2. Variation of efficiency with number of cell and droplet diameter.

a PC (Core 2 Duo 3GHz, 2GB RAM) is about 72 hours for each run.

Owing to the fact that the velocity gradient at the central core is higher than in the other regions, the grids were refined in this region.

3.2   Inlet Geometries

The operating principle of a hydrocyclone is based on centrifugal forces, nevertheless, the efficiency of separation can be affected by the inlet design. Fig. 3 illustrates the standard design (A) and four different inlet designs (B, C, D and E). In design #1 (see Fig. 3B) the involute single inlet configuration is used with the angle of 20° relative to the horizontal coordinate. Also, in design #2 (see Fig. 3C) the involute single inlet design with the development curve ending is used. Configuration of design #3 is considered based on the angel of inlet orifice (75°) with the hydrocyclone axis (see Fig. 3B). Design #4 creates a partially static screw which is placed at the end of the inlet orifice of the hydrocyclone (see Fig. 3E). All inlets have the same flow area and the inner diameter of the cross sections is 6 mm; all hydrocyclones have the same body geometries according to the standard design (see Fig. 1). These inlets have been used in previous works [7, 15] for solid-liquid hydrocyclones but there is no report of efficiency comparison in oil-water separation hydrocyclones.

3.3   Boundary and Operating Conditions

Tab. 1 depicts the inlet flow specifications (mixture of oil and water) of hydrocyclones. For the current simulation, the plug

velocity profile was applied as inlet boundary condition, the inlet flow rate was 20 L/min where 17 % exits the hydrocyclone through the overflow and the rest through the underflow (according to reported empirical data in a deoiling hydrocyclone, the split ratio is 17 % [14]). Moreover, the overflow orifice of the hydrocyclone is assumed to be fully open to the atmosphere. The wall boundaries are subject to the solid regions (no-slip condition) and the standard wall function is applied for turbulent flow near the wall.

A Cartesian coordinate system was applied for the numerical simulation. To obtain the pressure field inside the hydrocyclone, the semi-implicit pressure linked equations (SIMPLE) algorithm was used for combination of continuity and momentum equations for two phases [16]. The quadratic upstream interpolation for convective kinetics (QUICK) schemes was applied for the interpolation of the field variable from cell centers to faces of control volumes as it was reported to be useful for swirling flows [17, 18]. Simulations were carried out for about 70000 incremental steps and time steps were set to 0.001. The convergence criteria were set to 10^{-3} except for the continuity equation and the volumetric ratio of the oil phase, in which the criteria were 10^{-5}. An in-house numerical code based on the finite volume method was applied to investigate the flow structure and separation efficiency of a 40 mm diameter typical deoiling hydrocyclone. The criterion used to evaluate hydrocyclone performance is separation efficiency and defined as [19]:

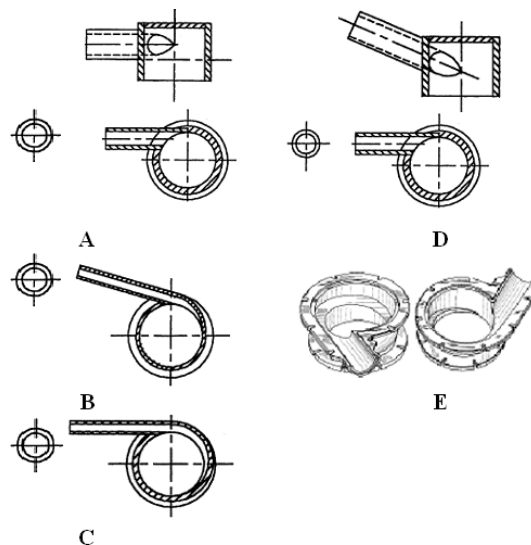$$E = \frac{a_o Q_o}{a_{in} Q_{in}} = 1 - \frac{a_u Q_u}{a_{in} Q_{in}} \tag{16}$$

Figure 3. Geometry of inlets: A) standard design, B) involute, design #1 [7], C) modified involute, design #2 [7], D) modified standard, design #3 [7], E) screw inlet, design #4 [15].

Table 1. Specifications of oil-water inlet flow to hydrocyclone at 20 °C.

Components	a_{in}	ρ (kg/m^3)	μ (kg/m s)
Oil	5 %	850	0.00332
Water	95 %	998	0.001

where E is the ratio of overflow oil flow rate to flow rate of oil in the cyclone feed.

4 Results and Discussion

4.1 Model Validation

It is necessary to validate the model and numerical code before their application for the analysis of flow through the modified hydrocyclone. Oil droplet size in the feed is one of the important parameters that change the performance of a LLHC design. Fig. 4 shows separation efficiency versus mean droplet diameter of oil in the feed inlet for the standard design of a typical deoiling hydrocyclone. The numerical simulations derived by two different drag coefficient correlations (see Eqs. (4) and (6)) were compared with the experimental results reported by Thew and Belaidi [14]. The error between experimental work and CFD simulation results decreases by about 4 % by using the modified drag coefficient (see Eq. (4)) in comparison with the results obtained using the Schiller-Naumann drag coefficient (see Eq. (6)). In the small diameter range of oil droplets, overprediction in comparison with the laboratory results is obtained with both drag coefficients (see

Eqs. (4) and (6)). This may be attributed to the fish hook effect occurring in centrifugal devices like hydrocyclones [4, 20], which is observed in the experimental work, promoting the drag forces and causing droplet breakage. The difference between the separation efficiency achieved in the simulation and in experimental work is more significant (about 17 %) for the mean droplet diameter range of 25–50 microns. This might be related to the higher computational error in this range. It seems that when using other turbulence models such as LES (large eddy simulation) this error can be reduced. But with the Reynolds stress method, a finer mesh density is needed that requires more computational time [21]. For droplet sizes above 50 microns the CFD simulations show good agreement with the experimental results and the difference in efficiency is 7 % less than the laboratory results. Therefore, the effect of inlet design and flow rate on the efficiency and flow structure was investigated in this range (the oil droplet diameter is equal to 70 μm) and the results were compared with those of the standard design.

4.2 Numerical Analysis of Standard Design

Fig. 5 shows the results for pressure distribution along the axial position of the hydrocyclone for steady simulation. As observed, the axial pressure distribution is maximum demonstrating the reversing flow point in the cyclone. Moreover, the overflow pressure gradient is much higher than the underflow pressure drop which illustrates more driving force for the reverse flow toward the overflow compared to the underflow at the core of the hydrocyclone. Fig. 6 illustrates the radial and axial distribution of pressure at a cross section of the hydrocyclone. The pressure difference in the radial direction causes the migration of the lighter phase (oil phase) to the central zone of flow. Fig. 7 depicts the distribution of volume fraction of the dispersed phase (oil) at a cross section of the hydrocyclone. This contour indicates the shift of the oil phase to the center of the hydrocyclone and the migration of the water phase to the wall due to the centrifugal force.

The effect of feed inlet velocity on the tangential velocity profile at different radial positions along the axis of the hydrocyclone in the cylindrical inlet chamber and conical reducing section is presented in Fig. 8A. The results demonstrate that an enhancement in feed velocity increases the tangential velocity at all radial positions, its maximum is near the walls and its minimum near the axis of the hydrocyclone at the cylindrical entrance chamber. The maximum of tangential velocity shifts to the core of the hydrocyclone by increasing the axial distance toward the underflow orifice. At any point on the radial position, with the promotion of tangential velocity, the centrifugal forces on the droplets increase and move the drops toward the hydrocyclone center. Fig. 8B presents the axial velocity profile at different positions from the top wall in the hydrocyclone. The negative axial velocities in-
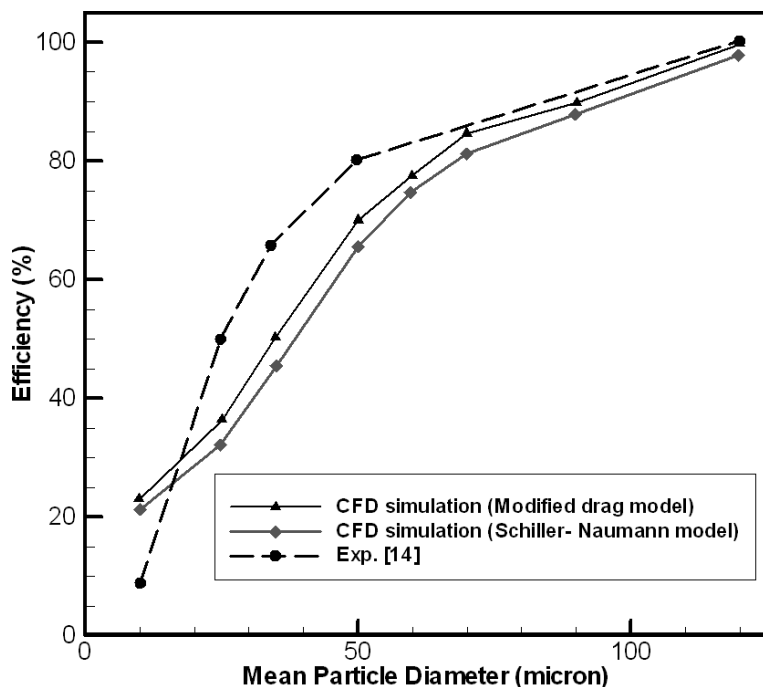
Figure 4. Comparison of experimental [14] and numerical simulation results for effect of oil droplet size on separation efficiency.
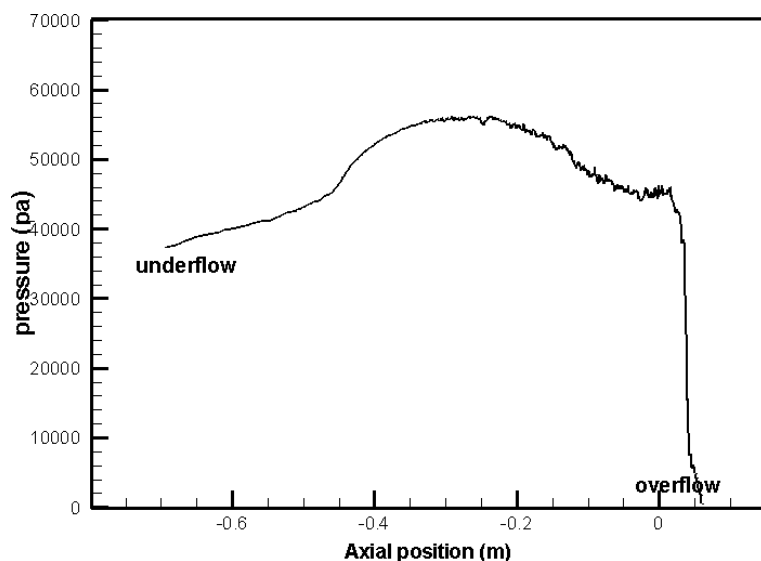
Figure 5. Static pressure of the mixture along the axis of hydrocyclone.

dicate backflow at the central zone of the hydrocyclone and the positive axial velocities cause downward flow near the hydrocyclone walls. The results clearly show that the backflow zone decreases from overflow to underflow.

4.3 Influence of Inlet Design on LLHC Efficiency

Fig. 9 illustrates the comparison between the tangential velocity at 20 mm distance from the top wall and 15 m/s inlet veloci-

ty for five different inlet designs (see Fig. 2). The average tangential velocity in designs #1 and #2 is higher than that of the standard design, which results in higher centrifugal forces and consequently an increase in separation efficiency for the wastewater clarification process. The inlet design configuration used in design #3 is the same as in the standard design but the inlet pipe makes an angle (15°) with the horizontal coordinate. The tangential velocity profile was derived almost in the same way as in the standard design. Thus, the horizontal variation of the inlet angle has more insignificant effects on the centrifugal forces in the hydrocyclone compared to the other designs. According to the results shown in Fig. 9, design #4 induces the highest tangential velocity.

Fig. 10 shows the efficiency curve (according to Eq. (16)) versus various inlet velocities for five different inlet designs. According to the results all four new inlet designs have higher efficiencies compared to the standard design. The difference between the LLHC efficiency with these inlets and the standard design can be improved by increasing the inlet velocity. As can be seen, the efficiencies of designs #1 and #2 are almost similar but the efficiencies of both designs are higher than those of the standard design in all ranges of inlet velocity. This might be related to the curvature form of the two inlets and causes reduction in wall stress which decreases energy consumption of the entrance fluid flow and makes the better symmetry to maintain a more stable reverse flow. These results demonstrate the favorable effect of the proposed modifications to inlets for the standard deoiling hydrocyclone de-

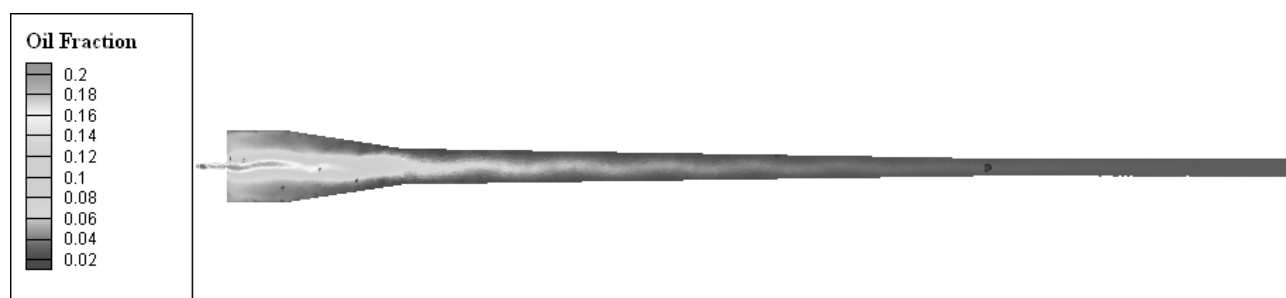**Figure 6.** Contour of static pressure (Pa) of standard hydrocyclone.

Figure 7. Distribution of dispersed phase (oil) volume fraction in standard hydrocyclone.
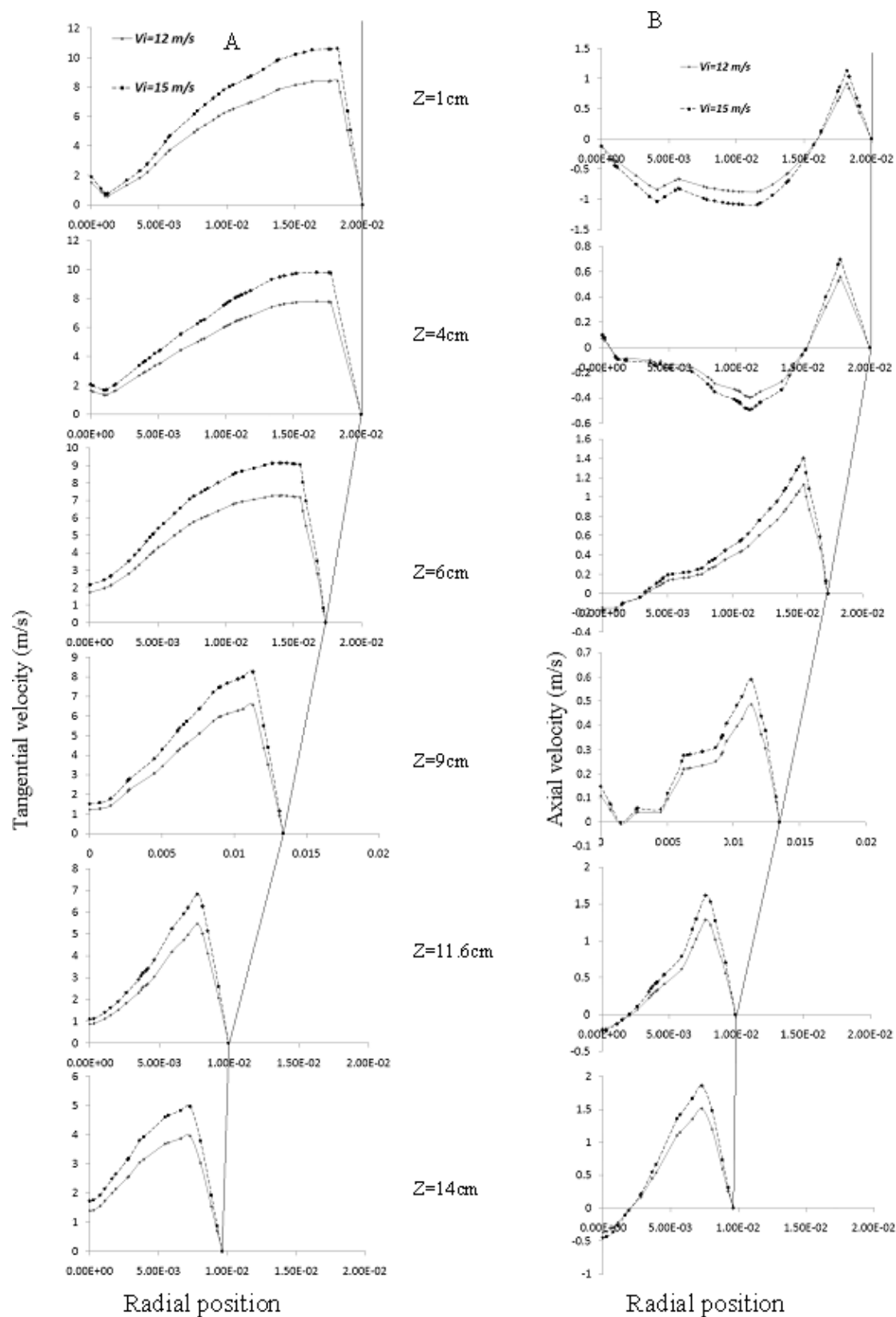
Figure 8. Tangential (A) and axial (B) velocity in radial position for two different inlet velocities (12 and 15 m/s) along the axis of hydrocyclone for continuous phase.
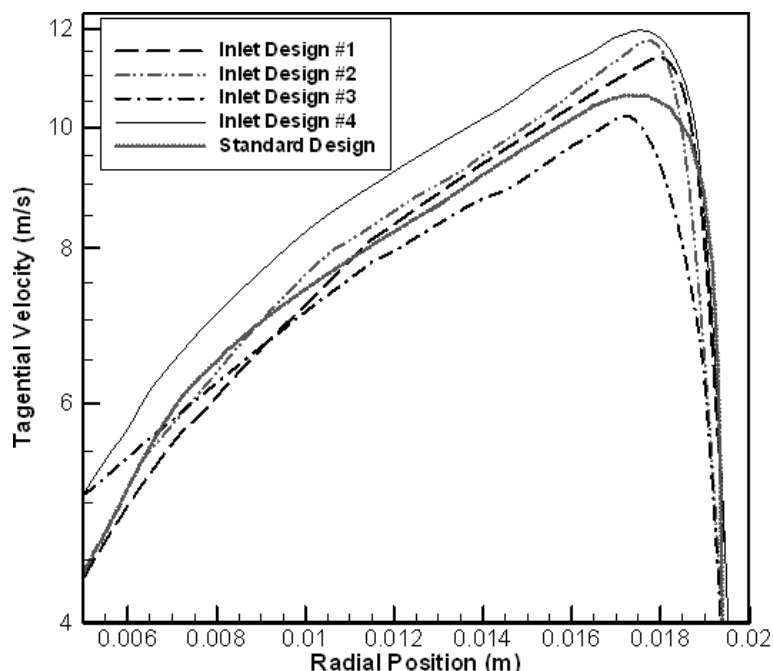
1892   S. Noroozi et al.

Chem. Eng. Technol. **2009**, *32*, No. 12, 1885–1893

Figure 9. Tangential velocity in radial position for various inlet designs at 20 mm from the top wall (inlet velocity of 15 m/s).
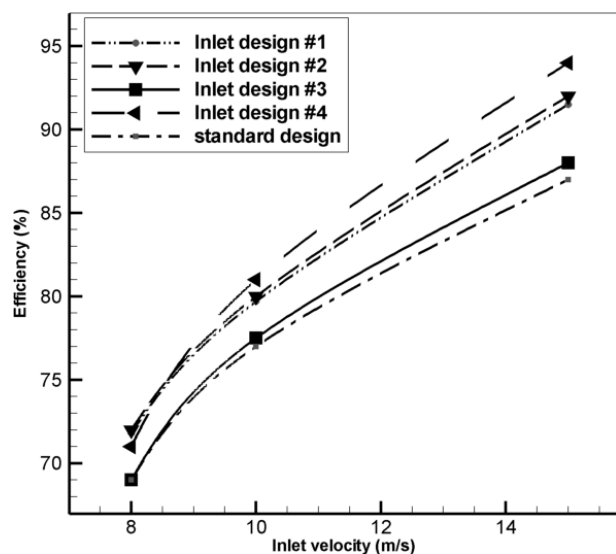

Figure 10. LLHC efficiency versus inlet velocity for various inlet designs and standard design at mean droplet diameter of 70 µm.

sign. According to Fig. 10 the separation efficiency of design #3 and the standard design are almost equal and the modification in inlet design shows no noticeable improvement in clarification performance. These results demonstrate that design #3 is not a good option for further experimental validation.

According to Fig. 9, the tangential velocity in design #4 in all ranges of radial position is higher than that in the standard design, which creates a higher average centrifugal force. Promotion of the tangential velocity can lead to a better clarification

process because the oil drops are driven to the core of the hydrocyclone at higher centrifugal forces. Fig. 10 shows that the separation efficiency of design #4 has a better phase separation capacity, especially at high inlet velocities (about 10 %). It may be related to the inlet helical structure that swirling in feed flow ist caused. This effect decreases wall drag and saves the entrance energy of the flow. The results demonstrate that this design is suitable for further experimental validation.

5 Conclusions

The influence of different inlet designs on de-oiling hydrocyclone efficiency was studied by CFD simulation. Two-phase liquid-liquid flow through the hydrocyclone was simulated with the Eulerian-Eulerian multiphase model and the RSM turbulence closure in steady flow was computed. The results demonstrate an acceptable agreement between the predictions of the CFD model and reported experimental work. Moreover, the modified drag correlation was proposed to estimate the drag force on droplets based on the Reynolds number and viscosity ratio of two phases and the results were compared with the CFD simulation using the Schiller-Naumann drag correlation. The simulations indicate an improvement in efficiency estimation by using the modified drag model in comparison with the Schiller-Naumann drag correlation. Furthermore, optimization of the separation performance by modifying the inlet design in the standard form of a typical deoiling hydrocyclone was achieved with the CFD methodology. Four inlet designs were simulated and the results compared with the simulation results of the standard configuration. According to the results obtained, the modified involute inlet type with longer screw curve or in case the inlet pipe has a horizontal angle shows approx. 7 % improvement in separation efficiency. Moreover, modification of the standard inlet design based on the angle of the inlet pipe (15°) with the horizontal axis does not improve separation efficiency. While the inlet flow is directed to the static screw channel in the hydrocyclone body, the results show a noticeable promotion in separation efficiency (about 10 %). This increment in oil-water separation efficiency is of prime importance in the oil industry.

Symbols used

d	[mm]	droplet diameter
D	[mm]	hydrocyclone diameter
E	[%]	deoiling efficiency
G_k	[J/s]	generation of turbulent kinetic energy
k	[–]	viscosity ratio (viscosity of droplet phase to viscosity of continuous phase)
L	[mm]	length

p	[N/m^2]	static pressure
Q	[L/min]	flow rate
R	[N]	Reynolds stress components
Re	[–]	Reynolds number
R_f	[%]	overflow split ratio (Q_o/Q_i)
T	[°C]	feed inlet temperature
u	[m/s]	velocity
x	[–]	coordinate axis
t	[s]	time

Greek letters

α	[%]	volume fraction
δ	[–]	Kronecker delta
ε	[J/s]	turbulent kinetic energy dissipation rate
κ	[J]	turbulent kinetic energy
μ	[kg/m s]	viscosity
ρ	[kg/m^3]	density
τ	[Pa]	stress strain tensor

Subscripts

c	continuous phase
d	dispersed phase
in	inlet orifice
i,j,k	directions in Cartesian coordinates
o	overflow orifice
u	underflow orifice
t	turbulent

Superscripts

‾	time average quantity
~	time fluctuation quantity
L	laminar
t	turbulence

The authors have declared no conflict of interest.

References

[1] D. A. Colman, *Ph.D. Thesis*, Southampton University, UK, **1981**.

[2] N. Meldrum, 19th Ann. Conf. on Offshore Technology, Houston **1987**.

[3] R. M. Changirwa, *Ph.D. Thesis*, Technical University of Nova Scotia, Canada, **1997**.

[4] S. A. Grady, G. D. Wesson, M. Abdullah, E. E. Kalu, *Filtr. Sep.* **2003**, *40 (9)*, 41. DOI: 10.1016/S0015-1882 (03)00930-3

[5] E. E. Paladino, G. C. Nunes, L. Schwenk, *Proc. of the Ann. Meeting*, AIChE, **2005**.

[6] S. Huang, *Can. J. Chem. Eng.* **2005**, *83*, 829. DOI: 10.1002/cjce.5450830504

[7] L. Y. Chu, W. M. Chen, X. Z. Lee, *Sep. Purif. Technol.* **2000**, *21*, 71. DOI: 10.1016/S1383-5866 (00)00192-1

[8] T. J. Olson, R. van Ommen, *Minerals Eng.* **2004**, *17*, 713. DOI: 10.1016/j.mineng.2003.12.008

[9] L. A. Rovinsky, *J. Food Eng.* **1995**, *26*, 131. DOI: 10.1016/0260-8774 (94)00019-6

[10] R. Delfos et al., *Minerals Eng.* **2004**, *17*, 721. DOI: 10.1016/j.mineng.2004.01.012

[11] E. Loth, *Int. J. Multiphase Flow* **2008**, *34*, 523. DOI: 10.1016/j.ijmultiphaseflow.2007.08.010

[12] A. Saboni, S. Alexandrova, *AIChE J.* **2002**, *48 (12)*, 2992. DOI: 10.1002/aic.690481225

[13] B. E. Launder, *Int. J. Num. Mech. Fluids* **1989**, *9 (8)*, 963. DOI: 10.1002/fld.1650090806

[14] A. Belaidi, M. T. Thew, *Trans. IChemE* **2003**, *81*, 305. DOI: 10.1205/02638760360596856

[15] B. L. Rogers, M. A. West, *US Patent D 464 067 S*, **2002**.

[16] H. K. Versteeg, W. Malalasekera, *An Introduction to Computational Fluid Dynamics*, 1st ed., Prentice Hall Publishing, Longman Group Ltd, Harlow, **1995**.

[17] J. Ko, S. Zahrai, O. Macchion, H. Vomhoff, *AIChE J.* **2006**, *52 (10)*, 3334. DOI: 10.1002/aic.10955

[18] K. U. Bhaskar et al., *Minerals Eng.* **2007**, *20*, 60. DOI: 10.1016/j.mineng.2006.04.012

[19] C. Gomez, J. Caldenty, S. Wang, *SPE J.* **2002**, *7*, 353.

[20] A. K. Majumder, H. Shah, P. Shukla, J. P. Barnwal, *Minerals Eng.* **2007**, *20*, 204. DOI: 10.1016/j.mineng.2006.10.002

[21] H. Shalaby, K. Pachler, K. Wozniak, G. Wozniak, *Int. J. Num. Methods in Fluids* **2005**, *48*, 1175, DOI: 10.1002/fld.942